

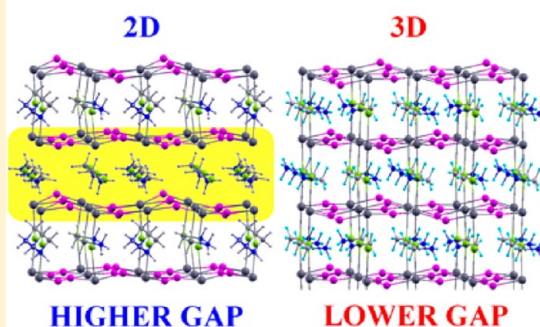
First-Principles Modeling of Mixed Halide Organometal Perovskites for Photovoltaic Applications

Edoardo Mosconi,^{*,†} Anna Amat,[†] Md. K. Nazeeruddin,[‡] Michael Grätzel,[‡] and Filippo De Angelis^{*,†}[†]Computational Laboratory for Hybrid/Organic Photovoltaics (CLHYO), CNR-ISTM, I-06123, Perugia, Italy[‡]Laboratory for Photonics and Interfaces, Institute of Chemical Sciences and Engineering, School of Basic Science, Swiss Federal Institute of Technology, CH-1015 Lausanne, Switzerland

S Supporting Information

ABSTRACT: We computationally investigate organometal $\text{CH}_3\text{NH}_3\text{PbX}_3$ and mixed halide $\text{CH}_3\text{NH}_3\text{PbI}_2\text{X}$ perovskites ($\text{X} = \text{Cl}, \text{Br}, \text{I}$), which are key materials for high efficiency solid-state solar cells. $\text{CH}_3\text{NH}_3\text{PbX}_3$ perovskites exhibited the expected absorption blue shift along the $\text{I} \rightarrow \text{Br} \rightarrow \text{Cl}$ series. The mixed halide systems surprisingly showed the $\text{CH}_3\text{NH}_3\text{PbI}_3$ and the $\text{CH}_3\text{NH}_3\text{PbI}_2\text{Cl}$ (or $\text{CH}_3\text{NH}_3\text{PbI}_{3-x}\text{Cl}_x$) perovskites to have similar absorption onset at ~ 800 nm wavelength, whereas $\text{CH}_3\text{NH}_3\text{PbI}_2\text{Br}$ absorbs light below ~ 700 nm. To provide insight into the structural and electronic properties of these materials, in light of their application as solar cell active layers, we perform periodic DFT calculations on the $\text{CH}_3\text{NH}_3\text{PbX}_3$ and $\text{CH}_3\text{NH}_3\text{PbI}_2\text{X}$ perovskites. We find a good agreement between the calculated band structures and the experimental trend of optical band gaps. For the mixed halide perovskites our calculations show the existence of two different types of structures with different electronic properties, whose relative stability varies by varying the X group. For these systems, the calculated formation energies decrease in the order $\text{I} > \text{Br} > \text{Cl}$, in line with the observed miscibility of $\text{CH}_3\text{NH}_3\text{PbI}_3$ and $\text{CH}_3\text{NH}_3\text{PbBr}_3$ compounds, while suggesting a comparatively smaller chlorine incorporation into $\text{CH}_3\text{NH}_3\text{Pb}(\text{I}_{1-x}\text{Cl}_x)_3$ compounds. We also show that Cl atoms preferentially occupy the apical positions in the PbI_4X_2 octahedra, while Br atoms may occupy both apical and equatorial positions, consistent with reported lattice parameters. The interplay of the organic and inorganic components of the perovskites, possibly mediated by hydrogen bonding between the ammonium groups and the halides, seems to be the key to the observed structural variability.

$\text{CH}_3\text{NH}_3\text{PbI}_2\text{X}$ Perovskites ($\text{X} = \text{I}, \text{Br}, \text{Cl}$)



1. INTRODUCTION

Dye-sensitized solar cells (DSCs) are promising hybrid/organic photovoltaic devices for high-efficiency and low-cost solar energy conversion,^{1–4} with a recently reported record power conversion efficiency exceeding 12%.⁵ In typical DSCs, a mesoporous film of TiO_2 nanoparticles is sensitized with light-harvesting molecular dyes which in most applications are surrounded by a redox mediator in an organic solvent.^{6,7} Substantial practical advantages can be envisaged by the replacement of the liquid electrolyte with a solid hole transporter material, with the development of highly efficient solid-state DSCs (S-DSCs) representing a possible pathway toward the large-scale uptake of this photovoltaic technology. The first work on S-DSCs was reported by Bach et al.⁸ who used spiro-MeOTAD (2,2',7,7'-tetrakis(*N,N*-di-*p*-methoxyphenylamine)-9,9'-spirobifluorene) as a solid hole conductor in place of the liquid electrolyte, with recently reported top efficiencies of devices employing molecular dyes of $\sim 7\%$.⁹

Several studies have been devoted to finding alternative sensitizers to the classically employed ruthenium dyes because of the relatively weak and scarcely tunable optical absorption of these sensitizers. Organic dyes^{10–12} or inorganic quantum dot

absorbers^{13,14} with high absorption coefficients have been intensively investigated, providing full sunlight absorption even in thin mesoporous TiO_2 layers. An appealing strategy to overcome the inherent limits of single molecular sensitizers is that of using an extremely thin (2–10 nm) inorganic semiconductor absorber. Power conversion efficiencies of 6.3% have been recently reported for this type of device based on Sb_2S_3 .¹⁵

Organic–inorganic hybrid $\text{CH}_3\text{NH}_3\text{PbX}_3$ ($\text{X} = \text{Br}, \text{I}$) perovskites have been introduced by Kojima et al.¹⁶ in 2009 as a new class of DSC sensitizing materials; in conjunction to a liquid electrolyte, a 3.8% power conversion efficiency was reported. In 2011, Im et al.¹⁷ obtained a 6.5% power conversion efficiency with the same type of materials, but the device was quickly corroded by electrolytes. In 2012 a related inorganic CsSnI_3 perovskite was used by Chung et al. as a hole conductor in S-DSCs based on ruthenium dyes, reaching 8.5% efficiency.¹⁸ After these initial works, the field of perovskite-based solar cells

Received: May 17, 2013

Revised: June 11, 2013

Published: June 13, 2013

has literally exploded, with extremely exciting very recent results. Kim et al. have demonstrated that $\text{CH}_3\text{NH}_3\text{PbI}_3$ perovskite/spiro-MeOTAD S-DSCs can reach a high photovoltaic efficiency of 9.7%.¹⁹ Etgar et al. showed that the $\text{CH}_3\text{NH}_3\text{PbI}_3$ perovskite/ TiO_2 heterojunction can form a 5.5% efficient solar cell without the use of a hole conductor.²⁰ The mixed halide $\text{CH}_3\text{NH}_3\text{PbI}_2\text{Br}$ perovskite was very recently employed together with TiO_2 nanowires to provide 4.9% power conversion efficiency.²¹ Chemically tuned $\text{CH}_3\text{NH}_3\text{Pb}(\text{I}_{1-x}\text{Br}_x)_3$ perovskites allowed Noh et al.²² to demonstrate colorful and stable hybrid solar cells with a reported photovoltaic efficiency of 12.3%. Heo et al.²³ reported 12% efficient $\text{CH}_3\text{NH}_3\text{PbI}_3$ perovskite/ TiO_2 S-DSCs based on a polymeric hole conductor.

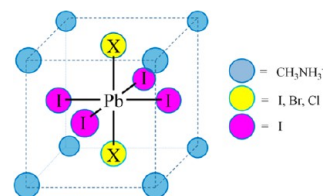
All the above results are based on TiO_2 as the electron-transporting medium. A recent breakthrough by Lee et al.²⁴ has demonstrated that the $\text{CH}_3\text{NH}_3\text{PbI}_2\text{Cl}$ perovskite, probably better defined as $\text{CH}_3\text{NH}_3\text{Pb}(\text{I}_{1-x}\text{Cl}_x)_3$,²⁵ can serve as *both* a light harvester *and* an electron conductor in meso superstructured solid state solar cells (MSSCs),²⁴ employing spiro-MeOTAD as the hole transporter. These devices, which notably do not employ a mesoporous TiO_2 photoanode and are therefore a new generation of hybrid solid-state photovoltaic devices, reached a remarkable 10.9% conversion efficiency.²⁴ The key to the MSSC efficiency is the high photocurrent of 17.8 mA/cm^2 , due to the extended perovskite absorption down to ca. 800 nm, and the high photovoltage of ca. 1 V, stemming from the crystalline nature of the perovskite electron conductor. Ball et al.²⁵ moved further and introduced a low-temperature Al_2O_3 processing which, together with a $\text{CH}_3\text{NH}_3\text{PbI}_{3-x}\text{Cl}_x$ perovskite, produced a 12.3% efficient MSSC and demonstrated a 9% efficient “flat-junction” thin-film solar cell, in which the perovskite absorber “performs the tasks of charge-separation and ambipolar charge transport of both carrier species”. A certified 14.1% efficient $\text{CH}_3\text{NH}_3\text{PbI}_3$ perovskite/ TiO_2 /spiro-MeOTAD was very recently presented by the Grätzel laboratory (http://www.nrel.gov/ncpv/images/efficiency_chart.jpg).

Despite the considerable and extremely fast progress in perovskite-based solid-state photovoltaics, some of the material aspects which are key to their functioning are not yet totally understood. As an example, the picture emerging from the experimental investigations discussed above surprisingly shows the $\text{CH}_3\text{NH}_3\text{PbI}_3$ and the nominally $\text{CH}_3\text{NH}_3\text{PbI}_2\text{Cl}$ perovskites to exhibit almost the same absorption onset ($\sim 800 \text{ nm}$),^{16,24} while the $\text{CH}_3\text{NH}_3\text{PbI}_2\text{Br}$ perovskite shows a blue-shifted absorption, with onset at $\sim 700 \text{ nm}$,²¹ qualitatively similar to what was found for the related $\text{CH}_3\text{NH}_3\text{PbX}_3$ ($\text{X} = \text{I} \rightarrow \text{Br} \rightarrow \text{Cl}$) materials.

From a structural point of view, we notice that some uncertainty seems to exist on the nature of the $\text{X} = \text{Cl}$ perovskite,²⁵ although the reported X-ray diffraction (XRD) data for this system have been interpreted as corresponding to a tetragonal structure, which is the established structure at room temperature for the $\text{CH}_3\text{NH}_3\text{PbI}_3$ perovskite.^{26,27} The structure of the orthorhombic phase of the $\text{CH}_3\text{NH}_3\text{PbI}_3$ perovskite was very recently solved, including the organic part,²⁷ while for the tetragonal $\text{CH}_3\text{NH}_3\text{PbI}_3$ perovskite structure some disorder of the organic moieties remains.²⁸ For the $\text{CH}_3\text{NH}_3\text{PbI}_2\text{Br}$ system two different structural assignments have been proposed based on XRD data, corresponding to a tetragonal²¹ or to a cubic phase.²² Furthermore, while for the mixed halide Cl-based perovskite the structural data are suggestive of chlorine atoms

lying at the apical positions of the PbI_4X_2 octahedron (Scheme 1), for $\text{X} = \text{Br}$ the structural data are compatible with various

Scheme 1. Schematic Illustration of the Perovskite Structure, Showing the PbI_4X_2 Octahedron with Equatorial I Atoms and Apical X Atoms



possible arrangements of bromine atoms, both at the apical and the equatorial positions (see below). Since the onset of optical absorption of the perovskites directly influences the light-harvesting capability of the solar cell photoanode, thus the short-circuit photocurrent density of the corresponding photovoltaic devices, understanding the origin of the different electronic properties of organometal halide perovskites from an atomistic, electronic structure point of view seems to us an important step toward a better understanding of this class of materials.

To provide further insight into the properties of organometal halide perovskites in relation to their potential application in photovoltaics, here we computationally investigate the structural and electronic properties of the experimentally characterized mixed halide $\text{CH}_3\text{NH}_3\text{PbI}_2\text{X}$ perovskites and of the related $\text{CH}_3\text{NH}_3\text{PbX}_3$ materials, with $\text{X} = \text{Cl}$, Br , and I . Although the nature and the composition of the $\text{CH}_3\text{NH}_3\text{PbI}_2\text{Cl}$ system is still uncertain,²⁵ we think it is anyways useful to model this system with the initially reported 2:1 iodine to chlorine ratio. Periodic DFT calculations employing experimental lattice parameters, and for selected cases including optimization of the cell parameters, have been performed to analyze the structural and electronic properties of the experimentally investigated materials. For the sake of comparison, we focus here on the tetragonal and cubic structures of the $\text{CH}_3\text{NH}_3\text{PbI}_2\text{X}$ and $\text{CH}_3\text{NH}_3\text{PbX}_3$ perovskites, respectively.

A large body of computational investigations were reported for various perovskite materials, but to the best of our knowledge no electronic structure calculations have been reported for the mixed halide $\text{CH}_3\text{NH}_3\text{PbI}_2\text{X}$ systems. Previous studies of relevance to our target include, but are possibly not limited to, periodic DFT and semiempirical calculations performed for the prototype $\text{CH}_3\text{NH}_3\text{PbI}_3$ perovskite^{27,29,30} and for the related $\text{CH}_3\text{NH}_3\text{SnX}_3$ and $\text{CH}_3\text{NH}_3\text{PbX}_3$ materials with $\text{X} = \text{Cl}$, Br , and I .^{31–34} Further computational analyses were devoted to the PbTiO_3 cubic perovskites³⁵ and to $\text{Sr}_{1-x}\text{Ba}_x\text{SnO}_3$ materials.³⁶ Also, a large series of perovskite materials for solar energy and solar fuels applications were computationally scrutinized.^{37–39}

2. COMPUTATIONAL DETAILS AND CALIBRATION

Periodic GGA-DFT calculations using the PBE exchange-correlation functional^{40,41} were performed on the tetragonal phase of the mixed halide $\text{CH}_3\text{NH}_3\text{PbI}_2\text{X}$ materials. For comparative purposes, we also performed calculations on the cubic phases of the related $\text{CH}_3\text{NH}_3\text{PbX}_3$ perovskites, with $\text{X} = \text{I}$, Br , and Cl . For the mixed halide perovskites, the tetragonal

simulation cell contains four repeated $\text{CH}_3\text{NH}_3\text{PbI}_2\text{X}$ units, while a single $\text{CH}_3\text{NH}_3\text{PbX}_3$ unit was considered for the cubic phases.

The PWSCF code as implemented in the Quantum-Espresso program package was used throughout.⁴⁰ Electron–ion interactions were described by ultrasoft pseudopotentials with electrons from Pb 5d, 6s, 6p; N and C 2s, 2p; H 1s; I 5s, 5p; Br 4s, 4p; and Cl 3s, 3s, shells explicitly included in the calculations. For Pb we used a scalar relativistic pseudopotential. A $4 \times 4 \times 4$ Monkhorst–Pack grid⁴² was chosen for sampling the Brillouin zone. Plane-wave basis set cutoffs for the smooth part of the wave functions and the augmented density of 25 and 200 Ry, respectively, were used. For the $\text{CH}_3\text{NH}_3\text{PbI}_3$ perovskite we also tested a $6 \times 6 \times 6$ and $8 \times 8 \times 8$ Monkhorst–Pack grid⁴² with 25/200 Ry cutoff, obtaining the same results in terms of relative stability and band gap than for the $4 \times 4 \times 4$ grid (see Table S1, Supporting Information). The $4 \times 4 \times 4$ k-point grid was therefore adopted for all the calculations. Additional tests on the $\text{CH}_3\text{NH}_3\text{PbI}_2\text{Cl}$ system were also performed with 35/240 Ry cutoffs, finding the same results in terms of relative stability and band gap as for the 25/200 Ry cutoffs which were therefore used for all the remaining calculations (see Table S2, Supporting Information). To check the importance of dispersion interactions in this class of systems, we performed selected calculations for the tetragonal $\text{CH}_3\text{NH}_3\text{PbI}_3$ perovskite using Grimme's DFT+D correction.⁴³ Geometry optimizations were performed for all structures employing available or estimated lattice parameters and checking their adequacy by performing atomic and lattice parameter optimizations for selected cases.

Since our aim here is to study the variation in structural and electronic properties, especially the band gap, for the investigated perovskites, some discussion about the accuracy of the employed computational methodology is required. Standard DFT-GGA calculations are usually shown to provide geometrical structures and relative stabilities for perovskites which are in good agreement with experimental data.^{31,33,35,38} Since these compounds are essentially ionic in nature, the cationic organic molecules interacting with the anionic inorganic matrix, we could expect electrostatic interactions, which are well described by DFT-GGA, to represent the main contribution to the interaction. This is indirectly confirmed by the usually good agreement between experimental and calculated structural parameters for this type of materials.²⁹ In this respect, the investigated perovskites are expected to be rather different from organic materials, for which van der Waals forces dominate the intermolecular interaction and are thus fundamental to determine the structure, cohesive energies, and the lattice parameters of these systems.^{44,45} Hydrogen bonds, which are possibly formed between the organic molecules and the halides, are usually well described by the employed PBE-GGA functional.⁴⁶ A partial assessment of the role of dispersion interactions in determining the structural and electronic properties of the $\text{CH}_3\text{NH}_3\text{PbI}_3$ perovskite is presented below.

A different situation is found for the calculated band gaps of various semiconducting materials, for which DFT-GGA calculations exhibit some erratic behavior. This is the case of, e.g., some transition metal oxides (a dramatic example is that of ZnO, for which an ca. 2.5 eV underestimation of the band gap is found by DFT-GGA) and in relation to the present studies also for binary ABO_3 perovskites, for which the standard PBE functional shows some underestimate of the band gap compared to the GLLB-SC functional, which provided an

average deviation of 0.5 eV compared to experimental values.³⁸ Hybrid DFT functionals, such as B3LYP or HSE06, or post-DFT methods (e.g., GW) usually show an improved agreement with experimental band gaps.^{37,47} In particular, Chiarella et al.³³ showed a sizably improved agreement between GW-calculated band gaps and experimental values for $\text{CH}_3\text{NH}_3\text{SnX}_3$ perovskites (X = Cl and Br) compared to GGA-DFT results. Also, a combination of GW and DFT methods allowed Berger et al. to develop an “ad hoc” correction to the band gap which brought calculated values for a series of perovskites within 0.2 eV from the corresponding experimental values.³⁷

Quite a peculiar situation seems to exist for Pb-based perovskites, for which DFT-GGA-calculated band gaps in general good agreement with experimental values have been reported. As examples, we mention that for $\text{CH}_3\text{NH}_3\text{PbI}_3$ calculated band gap values in the 1.3–1.6 eV range have been found,^{27,29,34} to be compared to an experimental band gap of ~ 1.55 eV.^{16,24} Also, for PbTiO_3 a 1.68 eV band gap was calculated, to be compared to the 1.70 eV experimental estimate.³⁵ Notably, such an agreement is not transferred to the in principle similar ASnX_3 (A = CH_3NH_3 or Cs) perovskites, for which DFT-GGA calculations provided a sizable underestimate of the band gap compared to experimental values.^{31–33} Interestingly, the ~ 2.3 eV band gap increase experimentally observed for CsSnCl_3 compared to CsSnI_3 perovskites ($1.3 \rightarrow 3.5\text{--}3.6$ eV)^{18,48} was almost quantitatively reproduced by DFT-GGA ($0.35\text{--}0.56 \rightarrow 2.85$ eV).³¹ Similarly, a band gap underestimate is found for BaSnO_3 and SrSnO_3 , but DFT-GGA results nicely reproduced the difference between the experimental band gaps of the two materials.³⁶ For the organometal $\text{CH}_3\text{NH}_3\text{SnX}_3$ perovskites, Chiarella et al.³³ reported a Br \rightarrow Cl band gap variation of 0.90 (1.54) eV by DFT-GGA (GW) calculations. The Br \rightarrow Cl band gap increase calculated by GW exactly matches the experimental band gap variation, with DFT-GGA underestimating the band gap variation but still providing a semiquantitatively correct picture of the halide substitution effect.

A further degree of complexity is introduced in Pb-based materials by relativistic effects,⁴¹ which are known to be particularly strong in lead.^{49,50} It was in particular reported that the inclusion of fully relativistic effects, e.g., spin–orbit coupling, reduces the band gap of PbO_2 by virtue of a sizable shift of the Pb unoccupied s–p shells.⁴⁷ Relativistic effects, with particular reference to spin–orbit coupling, have been earlier invoked to explain the electronic properties of CsSnX_3 compounds⁵¹ and more recently shown to affect the band structures of CsSnI_3 .⁵² Spin–orbit coupling was also recently found to be crucial for a correct description of Bi_2S_3 and Bi_2Se_3 electronic properties.⁵³ The reduction of the band gap introduced by spin–orbit coupling effects in Pb-based materials would be consistent with the large difference (~ 1 eV) calculated by DFT-GGA for the band gap of the CsSnI_3 and $\text{CH}_3\text{NH}_3\text{PbI}_3$ perovskites compared to the 0.25 eV experimental difference. In other words, it seems that the band gap of Sn- and Pb-based materials could be possibly underestimated by roughly the same amount by DFT-GGA, but the partial neglect in the calculations of relativistic effects, which are expectedly less important for Sn than for Pb, lead to increased band gaps for the Pb-based materials, bringing these values in closer agreement with experimental estimates. Future work will be devoted to precisely address this issue.

What seems to emerge from the above analysis is that DFT-GGA calculations reasonably, although fortuitously, reproduce

the band gaps of Pb-based perovskites, while substantially underestimating the band gap of Sn-based perovskites. Most important to our study, although the agreement on absolute values observed for the Pb-based materials is most likely due to error cancellation, band gap trends among different perovskites, with particular reference to the halide series, are at least semiquantitatively captured by standard DFT-GGA calculations, making us confident that the employed methodology is suitable to investigate the homologous series of $\text{CH}_3\text{NH}_3\text{PbI}_2\text{X}$ and $\text{CH}_3\text{NH}_3\text{PbX}_3$ materials, the subject of this study.

3. RESULTS AND DISCUSSION

As previously reported,²⁶ the $\text{CH}_3\text{NH}_3\text{PbI}_3$ perovskite shows a tetragonal crystal structure at room temperature, with lattice parameters of $a = b = 8.86$ Å and $c = 12.66$ Å. The $\text{CH}_3\text{NH}_3\text{PbI}_2\text{Br}$ perovskite has been assigned both a tetragonal structure with $a \sim b = 8.68$ and $c = 12.27$ ²¹ and a (pseudo) cubic structure with $a = b = c \sim 6.18$ Å;²² notice that the two data sets are quite comparable. $\text{CH}_3\text{NH}_3\text{PbI}_2\text{Cl}$ was reported as having a tetragonal structure with $a \sim b = 8.83$ Å and $c = 11.24$ Å.²⁴ The similar a – b lattice parameters reported for $\text{X} = \text{I}$ and Cl and the reduced c parameter observed going from $\text{X} = \text{I}$ to Cl could be suggestive of a structure in which the X groups may lie at the apical positions of the octahedron in the PbI_4X_2 structure (see Scheme 1). As a matter of fact, the ratio of the c lattice parameter between $\text{X} = \text{I}$ and Cl (1.13) is very similar to the ratio of lattice parameter for the cubic $\text{CH}_3\text{NH}_3\text{PbI}_3$ and $\text{CH}_3\text{NH}_3\text{PbCl}_3$ structures (1.11).²⁶ On the other hand, for the tetragonal $\text{CH}_3\text{NH}_3\text{PbI}_2\text{Br}$ perovskite structure the ratio of the c lattice parameter for $\text{X} = \text{I}$ and Br (1.03) slightly deviates from the ratio of the lattice parameter for the cubic $\text{CH}_3\text{NH}_3\text{PbI}_3$ and $\text{CH}_3\text{NH}_3\text{PbBr}_3$ structures (1.07) reported in ref 26. Moreover, in the case of a tetragonal structure, apical bromine atoms should induce a c lattice parameter close to that typical of the tetragonal structure for the $\text{CH}_3\text{NH}_3\text{PbBr}_3$ material, which is measured to be 11.83 Å.²⁶ By using the $c = 11.83$ Å parameter for the $\text{X} = \text{Br}$ case, the ratio between the c lattice parameter of $\text{X} = \text{I}$ and $\text{X} = \text{Br}$ is 1.07, which exactly matches the ratio of the lattice parameter for the cubic $\text{CH}_3\text{NH}_3\text{PbI}_3$ and $\text{CH}_3\text{NH}_3\text{PbBr}_3$ structures (1.07) reported in ref 26. This suggests a kind of disordered location of the Br anions in the crystal structures, with the possibility to find the bromine atoms both in the apical and in the equatorial octahedral positions.

3.1. Apical Substitution. For the $\text{CH}_3\text{NH}_3\text{PbI}_2\text{X}$ perovskites, we initially considered a tetragonal structure with the X groups lying at the apical octahedral positions, as depicted in Scheme 1, using the same $a = b = 8.86$ Å parameters and varying the c parameter. While for $\text{X} = \text{I}$ and Cl we used the c dimensions of the crystal structure of the corresponding materials (12.66 and 11.24 Å, as from refs 26 and 24, respectively), for $\text{X} = \text{Br}$ we performed calculations using two different lattice parameters, the corresponding structures hereafter labeled as A and B. In the A case we use the lattice cell parameters from the experimental XRD analysis of ref 21, $a = b = 8.68$ and $c = 12.27$ Å. For structure B, we used $a = b = 8.86$ Å, as for the $\text{X} = \text{I}$ and $\text{X} = \text{Cl}$ cases, but $c = 11.83$ Å as reported in ref 26 for the tetragonal $\text{CH}_3\text{NH}_3\text{PbBr}_3$ phase.

To check the adequacy of the employed cell parameters, for structure B of $\text{CH}_3\text{NH}_3\text{PbI}_2\text{Br}$ we also optimized the atomic coordinates and cell parameters (imposing 90° lattice angles), finding for the most stable structure (see below) a , b , and c parameters of 8.86, 8.80, and 11.80 Å, respectively, very similar to the starting lattice parameters. Also, structural and cell

parameter optimization was carried out for structure 1 of $\text{CH}_3\text{NH}_3\text{PbI}_3$, finding lattice parameters of 8.78, 8.74, and 12.70 Å, respectively, within 1% from experimental data. For the cubic $\text{CH}_3\text{NH}_3\text{PbX}_3$ structures the experimental lattice parameters of 6.33, 5.90, and 5.68 Å were used for $\text{X} = \text{I}$, Br , and Cl , respectively.²⁶ We recognize that the partial use of experimental lattice parameters could lead to some uncertainty in the calculated quantities, although we believe that the present modeling strategy should suffice for a comparative assessment of these materials, also in light of the partial structural and compositional information.

For the mixed halide perovskites, we set up a simulation cell consisting of four repeated $\text{CH}_3\text{NH}_3\text{PbI}_2\text{X}$ units, corresponding to the I4 space group, with two different initial orientations of the four organic molecules (head to head, 1, and head to tail, 2), lying parallel to the a – b plane (see Supporting Information). Upon geometry optimization a strong rearrangement of the organic molecules took place for all the investigated structures of type 1, leading to a rather disordered packing, while in structures of type 2 a higher order is maintained (see optimized structures in Figure 1). Structures of type 2 show the organic molecules in a head-to-tail arrangement lying almost parallel to the a – b plane, quite similar, in terms of the position of the organic moieties, to what is found in the crystal structure of the $\text{CH}_3\text{NH}_3\text{PbI}_3$ orthorhombic phase.²⁷ For $\text{CH}_3\text{NH}_3\text{PbI}_3$ the inorganic matrix of structure 1 closely resembles the crystal structure found for the tetragonal $\text{CH}_3\text{NH}_3\text{PbI}_3$ phase.²⁸

Interestingly, we also verified that exchanging the position of the organic molecules in the optimized geometries of 1 and 2, i.e., by inserting into the optimized inorganic structure of 1 the organic part of 2 and vice versa, led to an inversion of the structure, reverting 1 into 2 (see $\text{X} = \text{Cl}$ structures 1' and 2' in Figure 2), and consequently of the electronic properties (see below). These data confirm the relevant interplay between the organic and inorganic moieties in determining the overall stability and electronic properties of this class of materials.⁵⁴

We now move to analyze the electronic properties of the investigated systems. A summary of calculated relative stabilities and electronic band gap for the mixed halide $\text{CH}_3\text{NH}_3\text{PbI}_2\text{X}$ tetragonal structures and for the related $\text{CH}_3\text{NH}_3\text{PbX}_3$ cubic structures is reported in Table 1, along with the corresponding experimental band gap estimates. As mentioned above, the $\text{CH}_3\text{NH}_3\text{PbI}_3$ ¹⁶ and the $\text{CH}_3\text{NH}_3\text{PbI}_2\text{Cl}$ ²⁴ perovskites show similar absorption down to 800 nm wavelength (1.55 eV), whereas the $\text{CH}_3\text{NH}_3\text{PbI}_2\text{Br}$ perovskite absorbs light above 700 nm (1.78 eV).^{21,22} While it could be expected that the $\text{CH}_3\text{NH}_3\text{PbI}_2\text{Br}$ exhibits a more blue-shifted absorption spectrum than $\text{CH}_3\text{NH}_3\text{PbI}_3$ (recall that for the corresponding $\text{CH}_3\text{NH}_3\text{PbX}_3$ materials the band gap increases along the $\text{I} \rightarrow \text{Br} \rightarrow \text{Cl}$ series),^{16,55} simple chemical intuition would also predict $\text{CH}_3\text{NH}_3\text{PbI}_2\text{Cl}$ to show a blue-shifted absorption compared to $\text{CH}_3\text{NH}_3\text{PbI}_2\text{Br}$ and $\text{CH}_3\text{NH}_3\text{PbI}_3$, which is not experimentally observed (though we have to keep in mind the uncertain nature and composition of the $\text{CH}_3\text{NH}_3\text{PbI}_2\text{Cl}$ material).

As it can be noticed from Table 1, for $\text{X} = \text{I}$ and Cl structures 1 and 2 are characterized by small energy differences. These small energy differences are subject to some fluctuations with the level of theory (see Table S3, Supporting Information) and are probably below the accuracy of the employed computational setup; nevertheless, these results are useful to interpret some structure–property relations of these materials (see below). Notably, upon inclusion of dispersion interactions, for

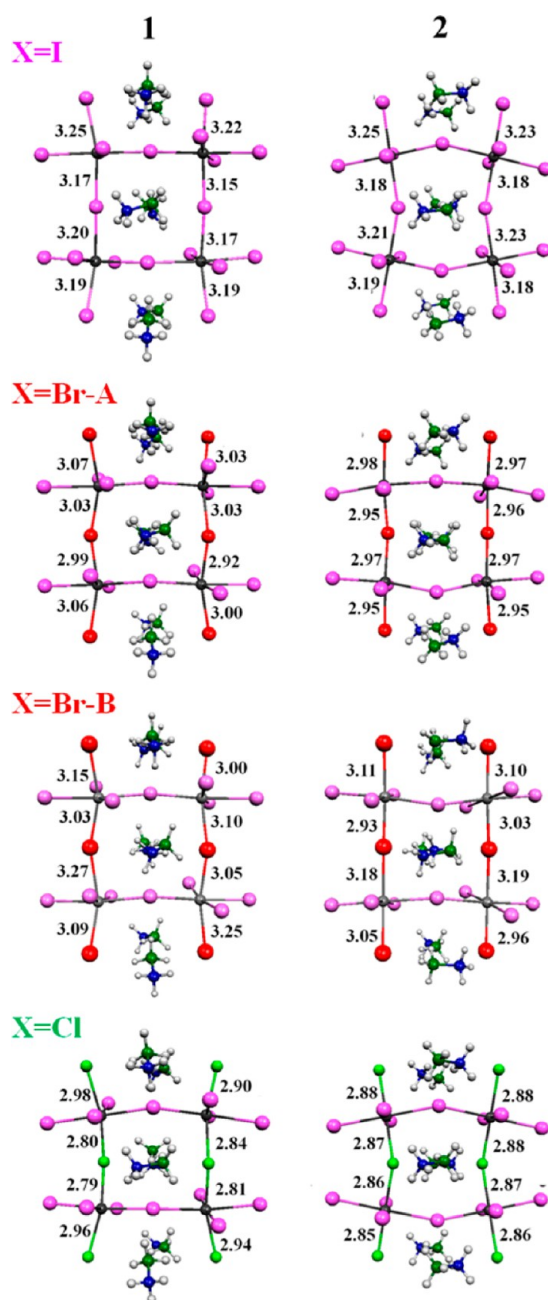


Figure 1. Optimized geometrical structures of type 1 (left) and 2 (right) for $\text{CH}_3\text{NH}_3\text{PbI}_2\text{X}$, for $\text{X} = \text{I}$, purple; $\text{X} = \text{Br}$, red; and $\text{X} = \text{Cl}$, green, along with main geometrical parameters. For $\text{CH}_3\text{NH}_3\text{PbI}_2\text{Br}$, the structures obtained by using the A and B lattice parameters are reported.

$\text{X} = \text{I}$ we still calculate structure 1 to be more stable than 2 by 0.03 eV, with a calculated band gap of 1.76 and 1.73 eV for 1 and 2, respectively, which is rigidly upshifted by 0.1 eV compared to the data in Table 1. For $\text{X} = \text{Br}$, larger energy differences are found within a given set of cell parameters. Also, structure 2A is only 0.03 eV more stable than structure 1B and features a similar band gap, despite the rather different employed cell parameters (see Table 1).

For the investigated mixed halide systems the top of the valence band is mainly composed by iodine p orbitals (bromine and chlorine states lying at slightly lower energy), while the conduction band is mainly contributed by lead p orbitals,

although some lead hybridization with halide states also takes place, in agreement with previous DFT results for the cubic, tetragonal, and orthorhombic $\text{CH}_3\text{NH}_3\text{PbI}_3$ phases;^{27,29} see Figure 3 for representative calculated density of states. All the calculated tetragonal mixed-halide systems show a direct band gap at the Γ point of the Brillouin zone (see Figure 4 and Supporting Information). A discussion of calculated band structures in relation to the band gap variation is reported in Section 3.3. Here we notice that for the investigated compounds the valence band is almost mirrored in the conduction band, in line with the ambipolar charge transport typical of these materials.^{18,24,25,52}

Interestingly, while for $\text{X} = \text{I}$ structures of type 1 and 2 lead to essentially the same band gap (1.66 and 1.63 eV), for $\text{X} = \text{Br}$ the 1A, 2A, and 1B structures give similarly higher band gap (1.87, 1.83, 1.89 eV, respectively), and the destabilized structure 2B exhibits a lower band gap (1.63 eV). Similarly, for $\text{X} = \text{Cl}$ a higher band gap is calculated for structure 1 compared to structure 2 (1.83 and 1.64 eV, respectively). Thus, for each of the three mixed halide systems, we find at least one structure (i.e., structures of type 2) with essentially the same band gap of ~ 1.63 eV, although the stability of such a structure type varies with the substituted halide. Although at first quite surprising, this result can be readily understood on the basis of the calculated electronic structure, showing in all cases the band gap to be contributed by iodine to lead states. In other words, the equatorial iodine atoms which are present also in the mixed halide systems roughly experience the same environment as in the $\text{CH}_3\text{NH}_3\text{PbI}_3$ structure, while the lead unoccupied states of lower energy are those hybridized with iodine, which being only partly perturbed by the presence of the axial bromine or chlorine atoms provide essentially the same electronic structure around the band gap for all three materials. We stress, however, that this result is to be taken with some care since in the real case both the lattice parameters and consequently the relative structure stability may vary.

For the cubic $\text{CH}_3\text{NH}_3\text{PbX}_3$ perovskites, our calculated data show the expected trend of increasing band gap going from $\text{X} = \text{I}$ to Br and Cl (Table 1), in line with experimental data,^{55,56} and for $\text{X} = \text{I}$ also with previous calculated band structures,^{27,29,34} providing for the $\text{X} = \text{I}$ cubic structure a band gap value almost matching the experimental one. Moving to the other $\text{CH}_3\text{NH}_3\text{PbX}_3$ perovskites, we notice that although the calculated band gaps follow the experimental trend a sizable underestimate of the band gap (by 0.8 eV) is retrieved by our calculations compared to experimental values for $\text{X} = \text{Cl}$, suggesting a possibly unbalanced description of the Cl-substituted species. A probably similar effect was also reported for the related $\text{CH}_3\text{NH}_3\text{SnX}_3$ perovskites.³³

Most notably, taking the more stable calculated tetragonal $\text{CH}_3\text{NH}_3\text{PbI}_2\text{X}$ structures for $\text{X} = \text{I}$ and Br, the experimentally observed optical band variation (1.55–1.78 eV) is accurately reproduced (1.66 to 1.87 eV), with a good agreement also on absolute values. Our results are therefore in line with previous DFT calculations, showing a nice, although as previously mentioned probably fortuitous, reproduction of the band gap for this class of materials.

As mentioned above, for the more stable $\text{CH}_3\text{NH}_3\text{PbI}_2\text{Cl}$ structure 2 we calculate a band gap of 1.64 eV, essentially identical to that of $\text{CH}_3\text{NH}_3\text{PbI}_3$. Recalling that for the cubic structures a sizable band gap underestimate was found for $\text{X} = \text{Cl}$, we cannot exclude that part of this problem is transferred to the mixed halide systems, leading to a fortuitous matching of

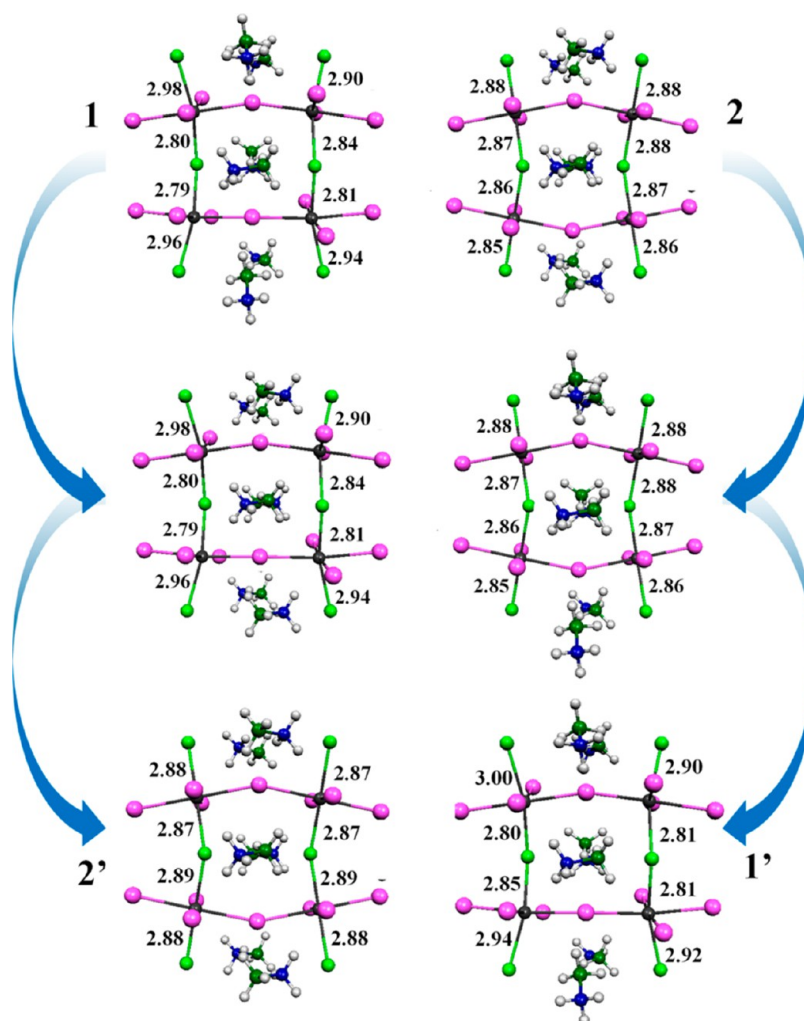


Figure 2. Optimized 1' and 2' structures of $\text{CH}_3\text{NH}_3\text{PbI}_2\text{Cl}$ are shown (bottom) and compared to structures 1 and 2 (top) and to the starting structures 1 and 2 with the inverted organic moieties (middle).

Table 1. Calculated Relative Stability and Band Gap (eV) for the Tetragonal Structures 1 and 2 of $\text{CH}_3\text{NH}_3\text{PbI}_2\text{X}$ and for the Cubic Structures of $\text{CH}_3\text{NH}_3\text{PbX}_3$, Using 25–200 Ry Plane-Wave Basis Set Cutoffs, Compared to Available Experimental Data^a

| tetragonal mixed halide structures | | | | | |
|--|--------------------|---------|-------------|----------------|---|
| CH ₃ NH ₃ PbI ₂ X | lattice parameters | struct. | rel. energy | calcd band gap | exptl band gap |
| X = I | a = b = 8.86 | 1 | 0.00 | 1.66 | 1.55 ^b –1.57 ^c |
| | c = 12.66 | 2 | 0.06 | 1.63 | |
| X = Br | a = b = 8.68 | 1A | 0.11 | 1.87 | 1.78 ^c |
| | c = 12.27 | 2A | 0.00 | 1.83 | |
| | a = b = 8.86 | 1B | 0.03 | 1.89 | |
| | c = 11.83 | 2B | 0.21 | 1.63 | |
| X = Cl | a = b = 8.86 | 1 | 0.03 (0.03) | 1.85 (1.83) | 1.55 ^d |
| | c = 11.24 | 2 | 0.00 (0.00) | 1.64 (1.64) | |
| cubic halide structures | | | | | |
| CH ₃ NH ₃ PbX ₃ | lattice parameters | --- | --- | calcd band gap | exptl band gap |
| X = I | a = 6.33 | --- | --- | 1.57 | 1.55 ^b |
| X = Br | a = 5.90 | --- | --- | 1.80 | 2.00 ^b , 2.33–2.35 ^{ef} |
| X = Cl | a = 5.68 | --- | --- | 2.34 | 3.11–3.12 ^{ef} |

^aThe employed lattice parameters are also reported. For X = Br and Cl the data refer to axial halide substitution. The boldface data refer to the more stable structure. For the tetragonal X = Cl structures, data in parentheses refer to calculated energetics and band gap using 35–240 Ry plane-wave basis set cutoffs. ^bIPCE onset from ref 16. ^cUV–vis spectral data from ref 21. ^dIPCE onset from ref 24. ^{e,f}UV–vis spectral data from refs 55 and 56. For structure 1 of X = I a band gap of 1.56 eV is calculated upon relaxing the structure and cell parameters.

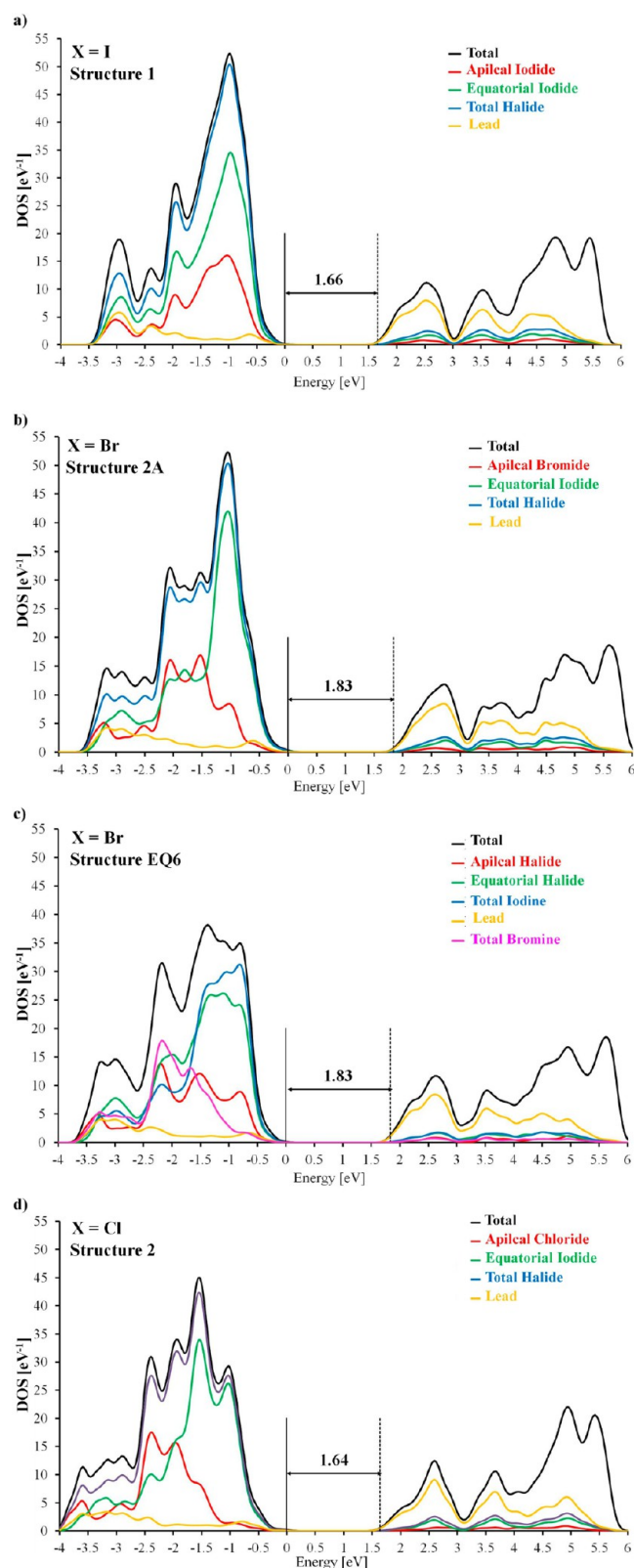


Figure 3. Calculated density of states (DOS) for the more stable species of $\text{CH}_3\text{NH}_3\text{PbI}_3$ (a), apical $\text{CH}_3\text{NH}_3\text{PbI}_2\text{Br}$ (b), equatorial $\text{CH}_3\text{NH}_3\text{PbI}_2\text{Br}$ (c), and $\text{CH}_3\text{NH}_3\text{PbI}_2\text{Cl}$ (d) perovskites.

the $\text{X} = \text{Cl}$ and I band gaps, although, as discussed above, a similar band gap can be somehow expected considering the calculated electronic structure. To further validate the accuracy of the employed methodology, a test using 35–240 Ry plane-

wave basis set cutoffs has been performed on the $\text{CH}_3\text{NH}_3\text{PbI}_2\text{Cl}$ system for structures 1 and 2, finding essentially the same relative stability and band gap (Table 1). This confirms that our results are stable with respect to basis set expansion. Furthermore, simultaneous optimization of atomic coordinates and of cell parameters was performed for the $\text{CH}_3\text{NH}_3\text{PbI}_2\text{Cl}$ system, finding the same band gaps for structures 1 and 2 as for the calculations employing the experimental lattice parameters, but structure 2 was favored by 0.09 eV compared to 1 (see Supporting Information). Notice also that excitonic effects are not included in our band structure calculations and that slightly higher exciton binding energies were found for $\text{CH}_3\text{NH}_3\text{PbBr}_3$ compared to $\text{CH}_3\text{NH}_3\text{PbI}_3$,⁵⁷ and possibly even higher for $\text{X} = \text{Cl}$, which could lead to further differences between the band gap values and the optical absorption spectra.

3.2. Equatorial Substitution. As previously mentioned, the reported XRD data for the $\text{X} = \text{Br}$ tetragonal structure shows a c lattice parameter of 12.27 Å,²¹ which is intermediate between the c lattice parameter of the tetragonal $\text{CH}_3\text{NH}_3\text{PbI}_3$ (12.66 Å) and $\text{CH}_3\text{NH}_3\text{PbBr}_3$ (11.83 Å) phases. Similarly, the estimated cubic structure lattice parameter (~ 6.18 Å) from ref 22 is intermediate between that of cubic $\text{CH}_3\text{NH}_3\text{PbI}_3$ (6.33 Å) and $\text{CH}_3\text{NH}_3\text{PbBr}_3$ (5.90 Å) structures. This suggests, for the tetragonal structure, the possibility of bromine to be located not only at the apical positions of the octahedron, as depicted in Scheme 1, but also in the equatorial plane (see Scheme 2). To further check this possibility, starting from the more stable 2A structure and maintaining the experimental lattice parameters, we alternatively exchanged the position of one Br atom with the four equatorial I atoms (see Scheme 2). By doing so, we obtained six structures for which relative stabilities and band gaps are reported in Table 2, where they are compared with the more stable apical-substituted structure 2A.

As we can see from Table 2, for $\text{X} = \text{Br}$ all structures generated by exchanging one apical bromine with one equatorial iodine atom are more stable than the 2A structure. Moreover, the calculated band gaps are similar for the calculated equatorial structures, lying in the range 1.81–1.87 eV, in agreement with the experimental value of 1.78 eV.²¹ Also the calculated band structure for the more stable equatorial structures (eq 3/eq 6) is rather similar to the more stable apical structure (2A).

On the contrary, for $\text{X} = \text{Cl}$, the exchange of one apical chlorine atom with one equatorial iodine atom leads for all the investigated structures to (slightly) higher energies and increased band gaps compared to the more stable structure 2 (see Table 2). Although these results were obtained employing the experimental lattice parameters, the picture extracted from our calculations suggests that for the tetragonal $\text{X} = \text{Br}$ structures there is a clear preference for structures where bromine is lying in both the apical and equatorial positions.

3.3. Origin of the Band Gap Variation. To explain the origin of the band gap variation observed for structures 1 and 2 in the investigated mixed halide systems, we went back to investigate the geometrical structures of the apical-substituted systems featuring the same $a = b$ lattice parameters (Figure 1). Notably, for structures A of the $\text{CH}_3\text{NH}_3\text{PbI}_2\text{Br}$ perovskite and for the corresponding equatorial structures, the different employed lattice parameters introduce a compression of the Pb–I distances and a structural distortion which leads to the observed band gap increase.

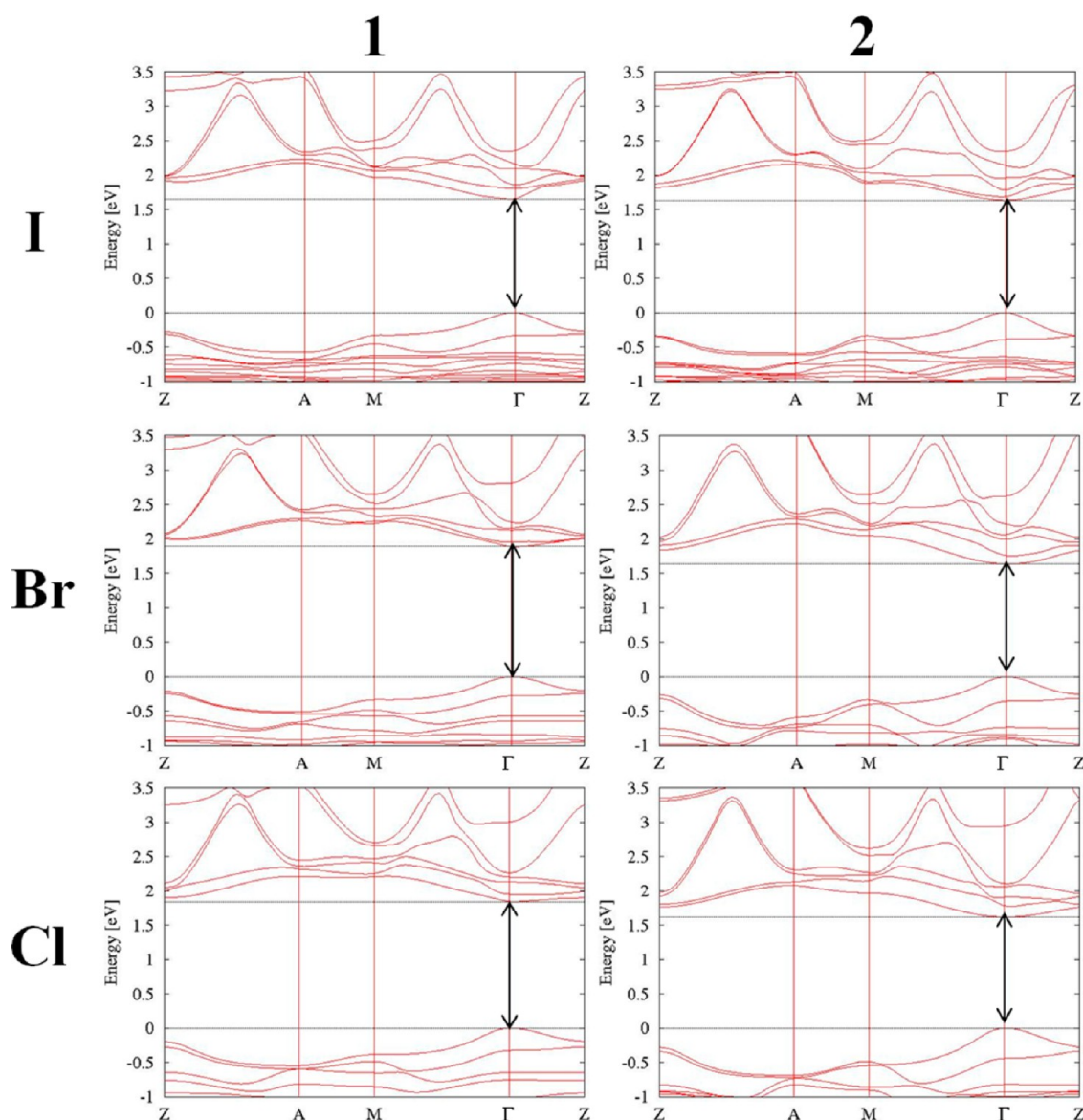


Figure 4. Calculated band structures along the $Z \rightarrow A \rightarrow M \rightarrow \Gamma \rightarrow Z$ directions for structures **1(B)**, left, and **2(B)**, right, for $\text{CH}_3\text{NH}_3\text{PbI}_2\text{X}$ of $X = \text{I}$ (Br) and Cl. The zero of the energy is set to the highest occupied state. The vertical double arrows indicate the band gap. Horizontal lines indicate the valence band maximum and conduction band minimum. Notice the band flattening in the $A \rightarrow M$ direction for structures **1** compared to **2** for $X = \text{Br}$ and Cl, which is not exhibited by $X = \text{I}$.

For the homologous **1(B)** structures of $X = \text{Cl}$ (Br), we find a partially layered structure, which is clearly signaled by the calculated long/short/short/long pattern of Pb–X axial distances (Figure 1). This is particularly evident for the $X = \text{Cl}$ case, for which we calculate Pb–Cl distances of 2.98–2.80–2.79–2.96 Å for structure **1**, while the corresponding Pb–Cl distances for structure **2** are 2.88–2.87–2.86–2.85 Å. This Pb–X bond length alternation is only marginally shown by $X = \text{I}$. To quantify the distortion characterizing structures of type **1**, we have calculated the ratio between the longest and the shortest Pb–X axial distances (Figure 1), finding values of 1.03, 1.08, and 1.07 for $X = \text{I}$, Br, and Cl, respectively. For structures **2(B)**, similar ratios of 1.02, 1.01, and 1.01 are calculated for $X = \text{I}$, (Br), and Cl, respectively.

Interestingly, the partially layered character of structures **1(B)** for $X = \text{Cl}$ (Br) is clearly reflected in the band structures of the investigated materials, which are compared in Figure 4.

As previously noticed by Umebayashi et al.,²⁹ a flattening of the band dispersion along the vertical directions of the Brillouin zone (BZ) was associated to the conversion from the 3D structure of $\text{CH}_3\text{NH}_3\text{PbI}_3$ to the 2D structure of $(\text{C}_4\text{H}_9\text{NH}_3)_2\text{PbI}_4$. For the present tetragonal structures the corresponding vertical directions in the BZ are identified as the $\Gamma \rightarrow Z$ and $A \rightarrow M$ directions (see Supporting Information for a sketch of the BZ).

A comparison of the band structures along these high-symmetry directions clearly shows a reduced band dispersion for the partly layered structures **1** compared to **2** for $X = \text{Cl}$ and Br, which is particularly evident for the conduction band, while for $X = \text{I}$ the two structures have a similar dispersion along the selected vertical BZ directions. As a matter of fact, almost zero dispersion is found for the conduction band along the $A \rightarrow M$ direction for structure **1** of $X = \text{Cl}$. The partial structural layering and the associated band structure data are in line with

Scheme 2. Schematic Representation of the Structures Generated by Alternatively Exchanging the Position of One Apical X (Br or Cl) Atom with One of the Four Equatorial I Atoms

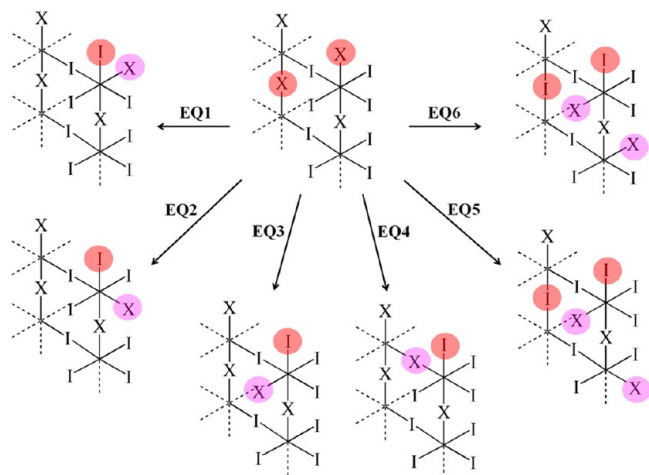


Table 2. Calculated Relative Stability and Band Gap (eV) for the Tetragonal X = Br and Cl Structures EQ1, EQ2, EQ3, EQ4, EQ5, and EQ6 Generated Exchanging the Position of One Apical X Atom with the Four Equatorial I Atoms (See Scheme 2)

| $\text{CH}_3\text{NH}_3\text{PbI}_2\text{Br}$ | relative energy | band gap |
|---|-----------------|----------|
| 2A | 0.00 | 1.83 |
| eq 1 | −0.09 | 1.81 |
| eq 2 | −0.04 | 1.87 |
| eq 3 | −0.10 | 1.84 |
| eq 4 | −0.01 | 1.86 |
| eq 5 | −0.08 | 1.83 |
| eq 6 | −0.10 | 1.83 |
| $\text{CH}_3\text{NH}_3\text{PbI}_2\text{Cl}$ | relative energy | band gap |
| 2 | 0.00 | 1.64 |
| eq 1 | +0.03 | 1.66 |
| eq 2 | +0.23 | 1.75 |
| eq 3 | +0.04 | 1.70 |
| eq 4 | +0.16 | 1.79 |
| eq 5 | +0.24 | 1.85 |
| eq 6 | +0.12 | 1.76 |

the observation that using larger organic molecules than methylammonium the structure of the corresponding RPbX_3 systems evolves toward a layered 2D structure, which is characterized by an increased band gap.^{54,55,58}

The reason for the different structural pattern and stability order observed by varying the X group is possibly related to the different halide size, with the larger iodine atoms creating a larger cavity for the organic molecules, which can at the same energy cost adopt the conformation leading to either structure 1 or 2. For X = Br we find a very similar stability for structure 2A and 1B, and their band gaps are in good agreement with the experimental measurements. Moreover, we have also demonstrated that bromine can be located in the apical as well as equatorial positions, providing a distribution of possible structures, which show essentially the same band gap, in agreement with available XRD and optical experimental data. On the other hand, chlorine atoms seem to be preferentially placed in the apical positions. The smaller Cl anions give rise to

a smaller cavity, which may induce the partly layered structure 1, with a consequent increase of the band gap and a slight structural destabilization.

To further evaluate the possible role of hydrogen bonding between the organic and inorganic moieties in determining the calculated structure and stability for the investigated systems, we report in Table 3 the minimum and average distances

Table 3. Hydrogen Bond Minimum and Average Distances (in Å) between the H of the Ammonium Groups and the Nearest Apical X Atoms

| X | minimum distance | | average distance | |
|-----------|--|------|------------------|------|
| | Apical X: CH ₃ NH ₃ ⁺ | | | |
| structure | 1 | 2 | 1 | 2 |
| I | 2.52 | 3.24 | 3.57 | 3.52 |
| Br | 2.33 | 3.13 | 3.43 | 3.38 |
| Cl | 2.12 | 2.95 | 3.25 | 3.35 |
| | Equatorial I: CH ₃ NH ₃ ⁺ | | | |
| structure | 1 | 2 | 1 | 2 |
| I | 2.58 | 2.56 | 3.01 | 2.74 |
| Br | 2.55 | 2.55 | 3.02 | 2.67 |
| Cl | 2.52 | 2.60 | 2.96 | 2.69 |

between the hydrogen ammonium atoms and the nearest apical X and equatorial I atoms. A graphical representation of the hydrogen bonds between ammonium hydrogen atoms and the apical and equatorial halide for the X = Cl species is shown in Figure 5. As we can see in Table 3 and Figure 5, structures of type 1 exhibit considerably smaller minimum H–X distances, confirming the presence of a specific interaction of one ammonium hydrogen with the X apical atoms, which is not found for structures 2, where all three ammonium hydrogen atoms show distances similar to the X halides. Moreover, for

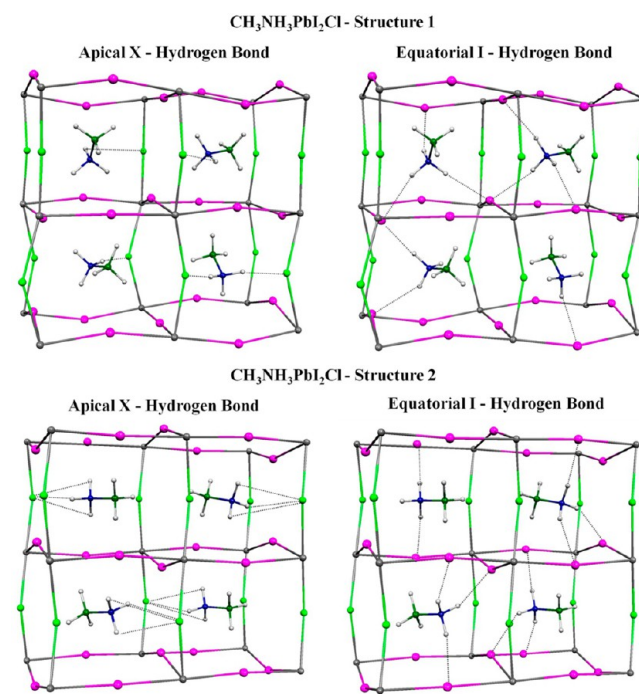
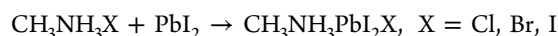


Figure 5. Structure 1 and 2 for $\text{CH}_3\text{NH}_3\text{PbI}_2\text{Cl}$. The hydrogen bonds between CH_3NH_3^+ and chlorine atoms (left) and equatorial iodine atoms (right) are shown.

structures of type 2, the average distance between the equatorial halides and the ammonium hydrogen atoms is smaller than in structures 1, indicating that the hydrogen bonds are also redistributed toward the equatorial I atoms, and this leads to preserving the 3D structures. For $X = \text{Br}$ and Cl the strong hydrogen bonds between the ammonium groups and the apical halide atoms typical of such systems⁵⁴ are formed in structures 1, inducing the partly layered geometries, with the consequent increasing of band gaps. For $X = \text{Br}$ and Cl , structures 2 maintain a 3D arrangement, and the layered structure is avoided by the hydrogen bonding which is present between the organic ammonium group and the halide apical and equatorial atoms of the inorganic moiety. For $X = \text{I}$ there is no asymmetry in the octahedral structure, and structures 1 and 2 maintain the 3D arrangement, resulting in essentially the same band gap.

Finally, based on the calculated total energies, we estimated the relative formation energies of the $\text{CH}_3\text{NH}_3\text{PbI}_2\text{X}$ perovskites as a function of the X group. We did this by subtracting from the total energies of the $\text{CH}_3\text{NH}_3\text{PbI}_2\text{X}$ perovskites the calculated total energies for the corresponding $\text{CH}_3\text{NH}_3\text{X}$ salts, which were separately determined by placing the neutral $\text{CH}_3\text{NH}_3\text{X}$ molecules in large cubic supercells with a minimum of 15 Å of vacuum in each direction. The relative formation energies for the investigated series are thus determined according to the following equation



which is related to the reaction employed to synthesize the materials. Since PbI_2 is a constant, we do not need to calculate its energy to evaluate the formation energies of the $X = \text{Br}$ and Cl materials relative to the $X = \text{I}$ system. By doing so, using the more stable eq 3/eq 6 structures found for $X = \text{Br}$, we calculate a formation energy for the tetragonal phase which is only 0.05 eV higher per $\text{CH}_3\text{NH}_3\text{PbI}_2\text{X}$ unit compared to that of $\text{CH}_3\text{NH}_3\text{PbI}_3$. This result is in line with the good miscibility of the $\text{CH}_3\text{NH}_3\text{PbI}_3$ and $\text{CH}_3\text{NH}_3\text{PbI}_2\text{Br}$ perovskites to form $\text{CH}_3\text{NH}_3\text{Pb}(\text{I}_{1-x}\text{Br}_x)$ materials characterized by a full range, i.e., $X = 0$ to 1, of intermediate compositions.²² For the more stable $X = \text{Cl}$ structure 2, we calculate a formation energy which is 0.16 eV higher per $\text{CH}_3\text{NH}_3\text{PbI}_2\text{X}$ unit compared to that of $\text{CH}_3\text{NH}_3\text{PbI}_3$, indicating that chlorine incorporation into the perovskite matrix is energetically disfavored compared to iodine and to bromine. These data are thus consistent with a composition of the type $\text{CH}_3\text{NH}_3\text{Pb}(\text{I}_{1-x}\text{Cl}_x)_3$ with quite small x , rather than with a 2:1 stoichiometry, as recently suggested.²⁵

4. CONCLUSIONS

Organometal halide perovskites are emerging as a new class of extremely powerful materials for photovoltaic applications, with published top device efficiency exceeding 12% and recently presented certified data above 14% efficiency. Despite the considerable and extremely fast progress in perovskite-based solid-state photovoltaics, some of the material aspects which are key to their functioning are not yet totally understood. In this work we focused on the mixed halide $\text{CH}_3\text{NH}_3\text{PbI}_2\text{X}$ perovskites ($X = \text{I}, \text{Br}$, and Cl), which are the most efficient materials to date. $\text{CH}_3\text{NH}_3\text{PbI}_3$ and $\text{CH}_3\text{NH}_3\text{PbI}_2\text{Cl}$ perovskites, the latter better described as $\text{CH}_3\text{NH}_3\text{Pb}(\text{I}_{1-x}\text{Cl}_x)_3$, have surprisingly been reported to exhibit almost the same absorption onset (~ 1.55 eV), while the $\text{CH}_3\text{NH}_3\text{PbI}_2\text{Br}$ perovskite shows an ca. 0.2 eV blue-shifted absorption. Since the onset of optical absorption of the perovskite absorbers

directly influences the light-harvesting capability of the photoelectrode, thus the short-circuit photocurrent density of the solar cell, understanding the origin of the different electronic properties of these materials seems an important step toward the full exploitation of this class of materials.

To provide further insight into the properties of organometal halide perovskites in relation to their potential application in photovoltaics, we thus computationally investigated the structural and electronic properties of the experimentally characterized mixed halide $\text{CH}_3\text{NH}_3\text{PbI}_2\text{X}$ perovskites by periodic DFT calculations. We found two stable structures with markedly different electronic properties, whose stability depends on the nature of the X halide. For $X = \text{I}$ the two types of structure provide essentially the same band gap, while sizable differences in stability and band gaps are calculated for $X = \text{Br}$ and Cl . Also, for $X = \text{I}$, the more stable calculated structure shows a head-to-tail position of the organic molecules, very similar to the crystal structure reported for the orthorhombic phase of this material.

Notably, the $\text{CH}_3\text{NH}_3\text{PbI}_2\text{Br}$ perovskite was found to show an increased band gap compared to $\text{CH}_3\text{NH}_3\text{PbI}_3$, in agreement with experimental evidence. For both materials, the calculated band gaps are within ~ 0.1 eV compared to experimental values. While the relative trends obtained by halide substitution are expected to be semiquantitatively described by DFT, the good agreement on absolute band gap values is most likely fortuitous and somehow limited to Pb-based materials, for which cancellation of errors due to neglect of spin-orbit coupling is likely to occur. Our calculations also provide similar band gaps for the $\text{CH}_3\text{NH}_3\text{PbI}_3$ and $\text{CH}_3\text{NH}_3\text{PbI}_2\text{Cl}$ perovskites, which can be explained by the calculated electronic structures. We have to recall however that the composition of the $\text{CH}_3\text{NH}_3\text{Pb}(\text{I}_{1-x}\text{Cl}_x)_3$ perovskite is still uncertain, and we cannot rule out some artificial lowering of the band gaps for Cl-substituted perovskites due to DFT-GGA shortcuts, as found for the cubic $\text{CH}_3\text{NH}_3\text{PbX}_3$ structures.

A sizable destabilization (0.16 eV) of the $\text{CH}_3\text{NH}_3\text{PbI}_2\text{Cl}$ perovskite structure compared to $\text{CH}_3\text{NH}_3\text{PbI}_2\text{Br}$ (0.05 eV) and $\text{CH}_3\text{NH}_3\text{PbI}_3$ (taken as a reference) was also calculated. These data are in agreement with the relative ease of formation of mixed $\text{CH}_3\text{NH}_3\text{Pb}(\text{I}_{1-x}\text{Br}_x)_3$ materials characterized by a full range of intermediate compositions, while it is suggestive of a reduced propensity of chlorine to be inserted into the $\text{CH}_3\text{NH}_3\text{PbI}_3$ lattice.

The interplay of the organic and inorganic perovskite components, mediated by hydrogen bonding between the ammonium groups and the halides, appears to be the key to such structural variability, which has important consequences for the different light-harvesting properties exhibited by these materials, thus for their photovoltaic performances.

■ ASSOCIATED CONTENT

Supporting Information

Additional calculations, figures, density of states, and band structures. This material is available free of charge via the Internet at <http://pubs.acs.org>.

■ AUTHOR INFORMATION

Corresponding Author

*E-mail: edoardo@thch.unipg.it; filippo@thth.unipg.it.

Notes

The authors declare no competing financial interest.

ACKNOWLEDGMENTS

We thank FP7-ENERGY-2010 Project ESCORT (contract No. 261920) and FP7-NMP-2009 Project SANS (contract No. 246124) for financial support.

REFERENCES

- O'Regan, B.; Grätzel, M. A Low-Cost, High-Efficiency Solar Cell Based on Dye-Sensitized Colloidal TiO_2 Films. *Nature* **1991**, *353*, 737–740.
- Grätzel, M. Photoelectrochemical Cells. *Nature* **2001**, *414*, 338–344.
- Grätzel, M. Solar Energy Conversion by Dye-Sensitized Photovoltaic Cells. *Inorg. Chem.* **2005**, *44*, 6841–6851.
- Grätzel, M. Recent Advances in Sensitized Mesoscopic Solar Cells. *Acc. Chem. Res.* **2009**, *42*, 1788–1798.
- Yella, A.; Lee, H.-W.; Tsao, H. N.; Yi, C.; Chandiran, A. K.; Nazeeruddin, M. K.; Diau, E. W.-G.; Yeh, C.-Y.; Zakeeruddin, S. M.; Grätzel, M. Porphyrin-Sensitized Solar Cells with Cobalt (II/III)-Based Redox Electrolyte Exceed 12% Efficiency. *Science* **2011**, *334*, 629–634.
- Nazeeruddin, M. K.; Kay, A.; Rodicio, I.; Humphry-Baker, R.; Mueller, E.; Liska, P.; Vlachopoulos, N.; Grätzel, M. Conversion of Light to Electricity by $\text{cis-X}_2\text{bis}(2,2'\text{-bipyridyl-4,4'-dicarboxylate})\text{-ruthenium(II)}$ Charge-Transfer Sensitizers ($\text{X} = \text{Cl}^-$, Br^- , I^- , CN^- , and SCN^-) on Nanocrystalline Titanium Dioxide Electrodes. *J. Am. Chem. Soc.* **1993**, *115*, 6382–6390.
- Nazeeruddin, M. K.; De Angelis, F.; Fantacci, S.; Selloni, A.; Viscardi, G.; Liska, P.; Ito, S.; Takeru, B.; Grätzel, M. Combined Experimental and DFT-TDDFT Computational Study of Photoelectrochemical Cell Ruthenium Sensitizers. *J. Am. Chem. Soc.* **2005**, *127*, 16835–16847.
- Bach, U.; Lupo, D.; Comte, P.; Moser, J. E.; Weissortel, F.; Salbeck, J.; Spreitzer, H.; Grätzel, M. Solid-State Dye-Sensitized Mesoporous TiO_2 Solar Cells with High Photon-to-Electron Conversion Efficiencies. *Nature* **1998**, *395*, 583–585.
- Snaith, H. J.; Petrozza, A.; Ito, S.; Miura, H.; Grätzel, M. Charge Generation and Photovoltaic Operation of Solid-State Dye-Sensitized Solar Cells Incorporating a High Extinction Coefficient Indole-Based Sensitizer. *Adv. Funct. Mater.* **2009**, *19*, 1810–1818.
- Mishra, A.; Fischer, M. K. R.; Bäuerle, P. Metal-Free Organic Dyes for Dye-Sensitized Solar Cells: From Structure: Property Relationships to Design Rules. *Angew. Chem., Int. Ed.* **2009**, *48*, 2474–2499.
- Pastore, M.; Mosconi, E.; Fantacci, S.; De Angelis, F. Computational Investigations on Organic Sensitizers for Dye-Sensitized Solar Cells. *Curr. Org. Synth.* **2012**, *9*, 215–232.
- Zeng, W.; Cao, Y.; Bai, Y.; Wang, Y.; Shi, Y.; Zhang, M.; Wang, F.; Pan, C.; Wang, P. Efficient Dye-Sensitized Solar Cells with an Organic Photosensitizer Featuring Orderly Conjugated Ethylenedioxythiophene and Dithienosilole Blocks. *Chem. Mater.* **2010**, *22*, 1915–1925.
- Rühle, S.; Shalom, M.; Zaban, A. Quantum-Dot-Sensitized Solar Cells. *ChemPhysChem* **2010**, *11*, 2290–2304.
- Mora-Seró, I. n.; Giménez, S.; Fabregat-Santiago, F.; Gómez, R.; Shen, Q.; Toyoda, T.; Bisquert, J. Recombination in Quantum Dot Sensitized Solar Cells. *Acc. Chem. Res.* **2009**, *42*, 1848–1857.
- Chang, J. A.; Im, S. H.; Lee, Y. H.; Kim, H.-j.; Lim, C.-S.; Heo, J. H.; Seok, S. I. Panchromatic Photon-Harvesting by Hole-Conducting Materials in Inorganic–Organic Heterojunction Sensitized-Solar Cell through the Formation of Nanostructured Electron Channels. *Nano Lett.* **2012**, *12*, 1863–1867.
- Kojima, A.; Teshima, K.; Shirai, Y.; Miyasaka, T. Organometal Halide Perovskites as Visible-Light Sensitizers for Photovoltaic Cells. *J. Am. Chem. Soc.* **2009**, *131*, 6050–6051.
- Im, J.-H.; Lee, C.-R.; Lee, J.-W.; Park, S.-W.; Park, N.-G. 6.5% Efficient Perovskite Quantum-Dot-Sensitized Solar Cell. *Nanoscale* **2011**, *3*, 4088–4093.
- Chung, I.; Lee, B.; He, J.; Chang, R. P. H.; Kanatzidis, M. G. All-Solid-State Dye-Sensitized Solar Cells with High Efficiency. *Nature* **2012**, *485*, 486–489.
- Kim, H.-S.; Lee, C.-R.; Im, J.-H.; Lee, K.-B.; Moehl, T.; Marchioro, A.; Moon, S.-J.; Humphry-Baker, R.; Yum, J.-H.; Moser, J. E. Lead Iodide Perovskite Sensitized All-Solid-State Submicron Thin Film Mesoscopic Solar Cell with Efficiency Exceeding 9%. *Sci. Rep.* **2012**, *2*, 591.
- Etgar, L.; Gao, P.; Xue, Z.; Peng, Q.; Chandiran, A. K.; Liu, B.; Nazeeruddin, M. K.; Grätzel, M. Mesoscopic $\text{CH}_3\text{NH}_3\text{PbI}_3/\text{TiO}_2$ Heterojunction Solar Cells. *J. Am. Chem. Soc.* **2012**, *134*, 17396–17399.
- Qiu, J.; Qiu, Y.; Yan, K.; Zhong, M.; Mu, C.; Yan, H.; Yang, S. All-Solid-State Hybrid Solar Cells Based on a New Organometal Halide Perovskite Sensitizer and One-Dimensional TiO_2 Nanowire Arrays. *Nanoscale* **2013**, *5*, 3245–3248.
- Noh, J. H.; Im, S. H.; Heo, J. H.; Mandal, T. N.; Seok, S. I. Chemical Management for Colorful, Efficient, and Stable Inorganic–Organic Hybrid Nanostructured Solar Cells. *Nano Lett.* **2013**, *13*, 1764–1769.
- Heo, J. H.; Im, S. H.; Noh, J. H.; Mandal, T. N.; Lim, C.-S.; Chang, J. A.; Lee, Y. H.; Kim, H.-j.; Sarkar, A.; Nazeeruddin, M. K. Efficient Inorganic–Organic Hybrid Heterojunction Solar Cells Containing Perovskite Compound and Polymeric Hole Conductors. *Nat. Photon.* **2013**, DOI: 10.1038/nphoton.2013.8.
- Lee, M. M.; Teuscher, J. I.; Miyasaka, T.; Murakami, T. N.; Snaith, H. J. Efficient Hybrid Solar Cells Based on Meso-Superstructured Organometal Halide Perovskites. *Science* **2012**, *338*, 643–647.
- Ball, J. M.; Lee, M. M.; Hey, A.; Snaith, H. J. Low-Temperature Processed Meso-Superstructured Thin-Film Perovskite Solar Cells. *Energy Environ. Sci.* **2013**, *6*, 1739–1743.
- Poglitich, A.; Weber, D. Dynamic Disorder in Methylammoniumtrihalogenoplumbates (II) Observed by Millimeter-Wave Spectroscopy. *J. Chem. Phys.* **1987**, *87*, 6373–6378.
- Baikie, T.; Fang, Y.; Kadro, J. M.; Schreyer, M.; Wei, F.; Mhaisalkar, S. G.; Grätzel, M.; White, T. J. Synthesis and Crystal Chemistry of the Hybrid Perovskite $(\text{CH}_3\text{NH}_3)\text{PbI}_3$ for Solid-State Sensitized Solar Cell Applications. *J. Mater. Chem. A* **2013**, *1*, 5628–5641.
- Kawamura, Y.; Mashiyama, H.; Hasebe, K. Structural Study on Cubic-Tetragonal Transition of $\text{CH}_3\text{NH}_3\text{PbI}_3$. *J. Phys. Soc. Jpn.* **2002**, *71*, 1694.
- Umebayashi, T.; Asai, K.; Kondo, T.; Nakao, A. Electronic Structures of Lead Iodide Based Low-Dimensional Crystals. *Phys. Rev. B* **2003**, *67*, 155405.
- Koutselas, I. B.; Ducasse, L.; Papavassiliou, G. C. Electronic properties of three- and low-dimensional semiconducting materials with Pb halide and Sn halide units. *J. Phys.: Condens. Matter* **1996**, *8*, 1217–1227.
- Borriello, I.; Cantele, G.; Ninno, D. Ab Initio Investigation of Hybrid Organic–Inorganic Perovskites Based on Tin Halides. *Phys. Rev. B* **2008**, *77*, 235214.
- Takahashi, Y.; Obara, R.; Lin, Z.-Z.; Takahashi, Y.; Naito, T.; Inabe, T.; Ishibashi, S.; Terakura, K. Charge-Transport in Tin-Iodide Perovskite $\text{CH}_3\text{NH}_3\text{SnI}_3$: Origin of High Conductivity. *Dalton Trans.* **2011**, 40, 5563–5568.
- Chiarella, F.; Zappettini, A.; Licci, F.; Borriello, I.; Cantele, G.; Ninno, D.; Cassinese, A.; Vaglio, R. Combined Experimental and Theoretical Investigation of Optical, Structural, And Electronic Properties of $\text{CH}_3\text{NH}_3\text{SnX}_3$ Thin Films ($\text{X} = \text{Cl}$, Br). *Phys. Rev. B* **2008**, *77*, 045129.
- Chang, Y. H.; Park, C. H.; Matsuishi, K. First-Principles Study of the Structural and the Electronic Properties of the Lead-Halide-Based Inorganic–Organic Perovskites $(\text{CH}_3\text{NH}_3)\text{PbX}_3$ and CsPbX_3 ($\text{X} = \text{Cl}$, Br , I). *J. Korean Phys. Soc.* **2004**, *44*, 889–893.
- Lv, H.; Gao, H.; Yang, Y.; Liu, L. Density Functional Theory (DFT) Investigation on the Structure and Electronic Properties of the Cubic Perovskite PbTiO_3 . *App. Catal. A* **2011**, *404*, 54–58.

- (36) Moreira, E.; Henriques, J. M.; Azevedo, D. L.; Caetano, E. W. S.; Freire, V. N.; Albuquerque, E. L. Structural and Electronic Properties of $\text{Sr}_2\text{Ba}_{1-x}\text{SnO}_3$ from First Principles Calculations. *J. Solid State Chem.* **2012**, *187*, 186–194.
- (37) Berger, R. F.; Neaton, J. B. Computational Design of Low-Band-Gap Double Perovskites. *Phys. Rev. B* **2012**, *86*, 165211.
- (38) Castelli, I. E.; Olsen, T.; Datta, S.; Landis, D. D.; Dahl, S.; Thygesen, K. S.; Jacobsen, K. W. Computational Screening of Perovskite Metal Oxides for Optimal Solar Light Capture. *Energy Environ. Sci.* **2012**, *5*, 5814–5819.
- (39) Vojvodic, A.; Nørskov, J. K. Optimizing Perovskites for the Water-Splitting Reaction. *Science* **2011**, *334*, 1355–1356.
- (40) Giannozzi, P.; Baroni, S.; Bonini, N.; Calandra, M.; Car, R.; Cavazzoni, C.; Ceresoli, D.; Guido, L. C.; Cococcioni, M.; Dabo, I.; et al. QUANTUM ESPRESSO: a Modular and Open-Source Software Project for Quantum Simulations of Materials. *J. Phys.: Condens. Matter* **2009**, *21*, 395502.
- (41) Perdew, J. P.; Burke, K.; Ernzerhof, M. Generalized Gradient Approximation Made Simple. *Phys. Rev. Lett.* **1996**, *77*, 3865–3868.
- (42) Monkhorst, H. J.; Pack, J. D. Special Points for Brillouin-Zone Integrations. *Phys. Rev. B* **1976**, *13*, 5188–5192.
- (43) Grimme, S. Semiempirical GGA-Type Density Functional Constructed with a Long-Range Dispersion Correction. *J. Comput. Chem.* **2006**, *27*, 1787–1799.
- (44) Nabok, D.; Puschnig, P.; Ambrosch-Draxl, C. Cohesive and Surface Energies of π -Conjugated Organic Molecular Crystals: A First-Principles Study. *Phys. Rev. B* **2008**, *77*, 245316.
- (45) Wong, B. M.; Ye, S. H. Self-Assembled Cyclic Oligothiophene Nanotubes: Electronic Properties from a Dispersion-Corrected Hybrid Functional. *Phys. Rev. B* **2011**, *84*, 075115.
- (46) Thanthiriwatte, K. S.; Hohenstein, E. G.; Burns, L. A.; Sherrill, C. D. Assessment of the Performance of DFT and DFT-D Methods for Describing Distance Dependence of Hydrogen-Bonded Interactions. *J. Chem. Theory Comp.* **2010**, *7*, 88–96.
- (47) Di Valentin, C.; Pacchioni, G.; Selloni, A. Electronic Structure of Defect States in Hydroxylated and Reduced Rutile TiO_2 (110) Surfaces. *Phys. Rev. Lett.* **2006**, *97*, 166803.
- (48) Voloshinovskii, A. S.; Myagkota, S. V.; Pidzyrailo, N. S.; Tokarivskii, M. V. Luminescence and Structural Transformations of CsSnCl_3 Crystals. *J. Appl. Spectrosc.* **1994**, *60*, 226–228.
- (49) Pyykko, P. Relativistic Effects in Structural Chemistry. *Chem. Rev.* **1988**, *88*, 563–594.
- (50) Ahuja, R.; Blomqvist, A.; Larsson, P.; Pyykkö, P.; Zaleski-Ejgierd, P. Relativity and the Lead-Acid Battery. *Phys. Rev. Lett.* **2011**, *106*, 018301.
- (51) Parry, D. E.; Tricker, M. J.; Donaldson, J. D. The Electronic Structure of CsSnBr_3 and Related Trihalides; Studies Using XPS and Band Theory. *J. Solid State Chem.* **1979**, *28*, 401–408.
- (52) Chung, I.; Song, J.-H.; Im, J.; Androulakis, J.; Malliakas, C. D.; Li, H.; Freeman, A. J.; Kenney, J. T.; Kanatzidis, M. G. CsSnI_3 : Semiconductor or Metal? High Electrical Conductivity and Strong Near-Infrared Photoluminescence from a Single Material. High Hole Mobility and Phase-Transitions. *J. Am. Chem. Soc.* **2012**, *134*, 8579–8587.
- (53) Filip, M. R.; Patrick, C. E.; Giustino, F. GW Quasiparticle Band Structures of Stibnite, Antimonite, Bismuthinite, and Guanajuatite. *Phys. Rev. B* **2013**, *87*, 205125.
- (54) Mitzi, D. B. Templating and Structural Engineering in Organic–Inorganic Perovskites. *J. Chem. Soc., Dalton Trans.* **2001**, 1–12.
- (55) Papavassiliou, G. C.; Koutselas, I. B. Structural, Optical and Related Properties of Some Natural Three- And Lower-Dimensional Semiconductor Systems. *Synth. Met.* **1995**, *71*, 1713–1714.
- (56) Kitazawa, N.; Watanabe, Y.; Nakamura, Y. Optical Properties of $\text{CH}_3\text{NH}_3\text{PbX}_3$ (X = halogen) and Their Mixed-Halide Crystals. *J. Mater. Sci.* **2002**, *37*, 3585–3587.
- (57) Tanakaa, K.; Takahashia, T.; Bana, T.; Kondoa, T.; Uchida, K.; Miura, N. Comparative study on the excitons in lead-halide-based perovskite-type crystals $\text{CH}_3\text{NH}_3\text{PbBr}_3$ $\text{CH}_3\text{NH}_3\text{PbI}_3$. *Solid State Commun.* **2003**, *127*, 619–623.
- (58) Calabrese, J.; Jones, N. L.; Harlow, R. L.; Herron, N.; Thorn, D. L.; Wang, Y. Preparation and Characterization of Layered Lead Halide Compounds. *J. Am. Chem. Soc.* **1991**, *113*, 2328–2330.